Check for updates

Heterogeneous photocatalysts: an overview of classic and modern approaches for optical, electronic, and charge dynamics evaluation

Hui Ling Tan, †*[a] Fatwa F. Abdi *[b] and Yun Hau Ng *[ac]

The functionality of a photoactive semiconductor (*i.e.*, photocatalysts, photoelectrodes, *etc.*) is largely dictated by three key aspects: (i) band gap; (ii) absolute potentials of the conduction band minimum and the valence band maximum; and (iii) bulk and surface charge carrier dynamics. Their relevance to governing the energetics and the photo(electro)chemical mechanisms of the semiconductor has prompted development of a multitude of characterization tools to probe the specific characteristic of the material. This review aims to summarize the current experimental techniques, including the conventional and the state-of-the-art tools, directed at examining the key aspects (i), (ii), and (iii) of semiconductors. Although not being exhaustive, this didactic review can be useful to apprise the research community of the sophisticated research tools currently available for characterization of photo(electro)catalyst semiconductors as well as to bridge the multidisciplinary knowledge.

Key learning points

(1) An understanding of the fundamental and key properties (*i.e.*, band gap, band edge positions, and bulk and surface charge carrier dynamics) that dictate the functionality of a semiconductor photo(electro)catalyst.

(2) Bridging of multidisciplinary knowledge on different experimental tools currently available for comprehensive studies on the optical, electronic, and charge properties of a semiconductor.

(3) Providing "one-stop-shop" for the various experimental techniques, including the standard and the state-of-the-art research tools, available for in-depth examination of the discrete key properties of a semiconductor.

(4) An understanding of the inherent limitations of a wide variety of spectroscopic, (photo)electrochemical, time-resolved, and frequency-resolved measurements.

(5) Recognizing the emerging *in situ*/*operando* measurement techniques for characterizing a semiconductor.

1. Introduction

The yearning for clean, sustainable, and renewable energy as well as environmental remediation has instigated tremendous research interest in photo(electro)catalysis, which is a robust process for harvesting sunlight as the primary energy source. The burgeoning fields of photo(electro)catalysis include water splitting for H_2 generation, CO_2 reduction into organic fuels, and organic degradation for environmental pollutant abatement. An appropriate semiconductor, be it organic or inorganic material, is simply needed to bring about the desirable photo(electro)chemical reaction. Apart from being cost-effective and environmentally benign, the practicability of a semiconductor for targeted applications mostly relies on the solar energy conversion efficiency of the material. Recent advancement in photo(electro)catalysis mainly places emphasis on the strategies to enhance light absorption, suppress charge recombination, and improve the charge utilization of the semiconductor so that the solar energy conversion efficiency is optimized. These emergent approaches include semiconductor modification *via* doping, metal/co-catalyst loading, composite structure, defect induction, crystal facet engineering, and morphological control.[1]

Fundamentally, the overall efficiency of a semiconductor is dictated by three key intrinsic characteristics of the material:

[a] *Particles and Catalysis Research Group, School of Chemical Engineering, The University of New South Wales, Sydney, NSW 2052, Australia*

[b] *Helmholtz-Zentrum Berlin für Materialien und Energie GmbH, Institute for Solar Fuels, Hahn-Meitner-Platz 1, Berlin 14109, Germany. E-mail: fatwa.abdi@helmholtz-berlin.de*

[c] *School of Energy and Environment, City University of Hong Kong, Hong Kong SAR. E-mail: yunhau.ng@cityu.edu.hk*

† Present address: Department of Applied Chemistry, Faculty of Engineering, Kyushu University, Nishi-ku, Fukuoka 819-0395, Japan. E-mail: hui.ling.tan.291@m.kyushu-u.ac.jp

This journal is © The Royal Society of Chemistry 2019

Chem. Soc. Rev., 2019, **48**, 1255–1271 | 1255

(i) energy difference between the conduction band minimum (E_{CB}) and the valence band maximum (E_{VB}), that is, the band gap (E_g); (ii) absolute potentials of the E_{CB} and E_{VB} (*i.e.*, the band position); and (iii) dynamics of the photogenerated electrons and holes such as diffusion length, mobility, and lifetime as well as the rates of surface charge recombination and interfacial charge transfer. These aspects are schematically depicted in Fig. 1. The E_g limits the portion of the solar spectrum that can be utilized to activate the semiconductor (*i.e.*, semiconductors with $E_g >$ 3.0 eV are only responsive toward ultraviolet light, whereas those with smaller band gaps are favorable for more proficient solar energy harvesting). The E_{CB} and E_{VB} potentials define the respective reductive and oxidative powers of the electrons and holes generated upon photoexcitation of the semiconductor. From the thermodynamic point of view, the E_{CB} has to be higher
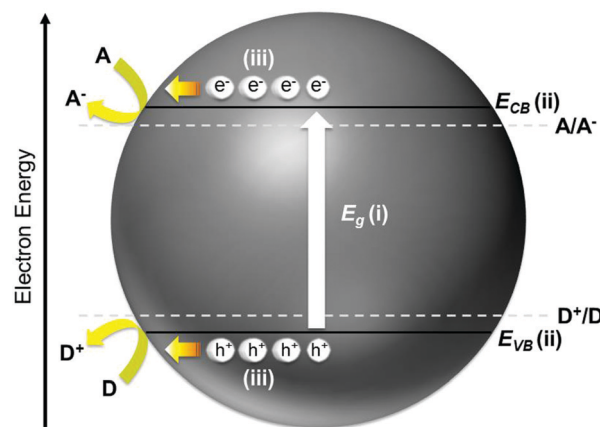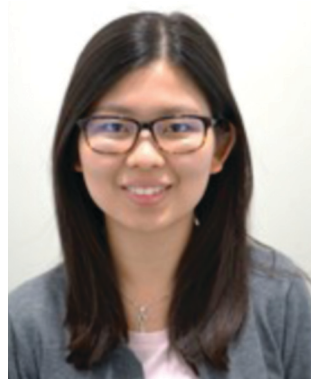

Fig. 1 The key aspects that govern the photo(electro)chemical efficiency of a semiconductor photocatalyst.

(more negative) than the reduction potential of A/A$^-$ to enable reduction of the electron acceptor, whereas the E_{VB} needs to be lower (more positive) than the oxidation potential of D$^+$/D to drive the oxidation of the electron donor. The dynamics of the photoinduced electrons and holes are equally important as they determine the number and efficiency of the charge carriers remaining active to partake in the interfacial reactions at the semiconductor/solution phase boundary in competition with charge recombination.

Determining all the aforementioned aspects is therefore of paramount importance; this will allow us to comprehend the charge energetics, to predict and understand the basic photo(electro)chemical mechanisms, and to exploit the full potential of a semiconductor, particularly for the development of new photo(electro)catalysts. However, in many studies, these properties (*i.e.*, E_g, E_{CB} and E_{VB} levels, and the charge carrier dynamics of the semiconductor) are often obtained from theoretical prediction or by simply adopting values from the

Hui Ling Tan

Hui Ling Tan received her Bachelor of Engineering degree in Chemical Engineering and PhD degree in Chemical Engineering from the University of New South Wales (UNSW) in 2012 and 2017, respectively. She was a postdoctoral research associate in the School of Chemical Engineering, UNSW. She is now in the Department of Applied Chemistry, Faculty of Engineering at Kyushu University as a Japan Society for the Promotion of Science (JSPS) Postdoctoral Fellow. Her research interests primarily focus on the design and fabrication of metal oxide and carbon-based materials for solar energy conversion applications.

Fatwa F. Abdi

Fatwa Abdi is a senior scientist and a group leader at the Institute for Solar Fuels, Helmholtz-Zentrum Berlin (HZB). He obtained his bachelor degree in 2005 from Nanyang Technological University and master's degree in 2006 from National University of Singapore and Massachusetts Institute of Technology, all in Materials Science and Engineering. After a short stint in the semiconductor industry, he pursued a PhD at TU Delft, the Netherlands, and graduated cum laude in 2013. He was the recipient of the Singapore-MIT Alliance fellowship (2005) and Martinus van Marum prize (2014) from the Royal Dutch Society of Sciences and Humanities. His research focuses on the development of solar energy conversion materials and devices.

Yun Hau Ng

Yun Hau Ng received his PhD from Osaka University, Japan, in 2009. After a brief research visit to the Radiation Laboratory at the University of Notre Dame (USA), he joined the ARC Centre of Excellence for Functional Nanomaterials at the UNSW with the Australian Postdoctoral Fellowship (APD). He became a lecturer (2014) and senior lecturer (2016) at the School of Chemical Engineering, UNSW. He is currently an associate professor at the School of Energy and Environment, City University of Hong Kong. His research is focused on the development of novel photoactive semiconductors for sunlight energy conversion. He received the Honda–Fujishima Prize in 2013 and the Distinguished Lectureship Award from the Chemical Society of Japan in 2018.

1256 | *Chem. Soc. Rev.*, 2019, 48, 1255–1271

This journal is © The Royal Society of Chemistry 2019

literature rather than being directly evaluated experimentally. This may lead to erroneous results, since these properties are known to depend on the specific material composition and/or surface structure.

With the interdisciplinary nature of the photo(electro)catalysis field, numerous characterization methods, particularly those with high sensitivity, selectivity, spatial, temporal, and spectral resolutions, have been greatly developed in the past few decades targeting at the photochemistry, physical chemistry, surface science, and materials science of semiconductor photocatalysts. These methods have been described in the literature, but reports are segregated and usually incomprehensive. This review aims to recapitulate standard and state-of-the-art characterization approaches, although non-exhaustive, for experimental determination of the discrete key properties (i)–(iii) of a semiconductor photo(electro)catalyst. Sections 2 and 3 of this paper cover the determination techniques for E_g and band edge positions, respectively. A brief account of the electronic properties of a semiconductor in the bulk, and at the surface and interface is incorporated in Section 3 to facilitate an understanding of their relevance in E_{CB} and E_{VB} analyses. Section 4 discusses the methods associated with the measurement of charge carrier dynamics both in the bulk and at the semiconductor surface. Finally, the development of combinatorial/ *in situ* characterization techniques to overcome the limitations of the instrumental techniques reviewed in Sections 2–4 is also presented in Section 5.

2. Band gap

Given that the E_g of a semiconductor photo(electro)catalyst fundamentally determines the light absorption ability and the resulting solar conversion efficiency of the material, E_g evaluation is indispensable in the design and development of photo(electro)catalysts. While there are various methods to attain the E_g value of a semiconductor, including electrical conductivity, Hall constant, and photoconductivity measurements, optical methods are by far the most widely employed techniques. Unlike the dependence of electrical conductivity and Hall constant analyses on temperature variation and the uncertainties of photoconductivity associated with surface states, characterization using optical spectroscopies is facile and straightforward to probe the electronic transitions of a solid based on the observed optical absorption or luminescence.

Of the manifold optical spectroscopic techniques, ultraviolet-visible (UV-vis) diffuse reflectance spectroscopy is the most frequently used, particularly for thin films and powdered materials. Typically, optical excitation of valence band electrons to the conduction band contributes to an abrupt increase in absorbance at a given wavelength corresponding to the E_g of the semiconductor. An investigation of the tail of the absorption curve of a semiconductor revealed that it exhibits a simple exponential drop. The onset of this drop (which is also the onset of the linear increase in absorption; point A in Fig. 2) has thereafter been identified as the absorption edge. Fochs estimated the E_g of various powdered semiconductors *via* the onset
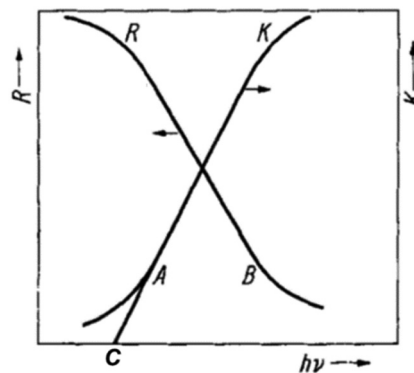

Fig. 2 Illustration of different onsets/points in diffuse reflectance (R) and absorption (K) spectra that are employed for E_g determination. Reproduced from ref. 2 with permission from WILEY-VCH Verlag GmbH & Co. KGaA, Weinheim, copyright 1970.

of the linear increase in diffuse reflectance (R), denoted as point B in Fig. 2. On the other hand, Shapiro determined E_g as the point of intersection between the line extrapolating the linear portion of the absorption curve and the wavelength axis (point C in Fig. 2). These two approaches, however, were argued by Tandon and Gupta to not reflect the onset of the absorption edge as accurate as that of using the point at which the linear increase in absorption starts (*i.e.*, point A).[2]

In addition to the conventional graphic representations (*i.e.*, plot of reflectance or absorbance against wavelength) discussed above, numerous empirical relations have also been derived to model the optical absorption edge of semiconductors that result in a range of equations being utilized for the graphical analysis of E_g in the literature. The most common expression being used to date is the one proposed by Tauc, Davis and Mott:[3,4]

$$(\alpha h\nu)^{1/n} = A(h\nu - E_g) \tag{1}$$

where α is the absorption coefficient, h is the Planck constant, ν is the light frequency, A is the proportional constant, and n may be taken as the value of 1/2, 3/2, 2, or 3 depending on the nature of the sample electronic transition (*i.e.*, direct allowed transition, direct forbidden transition, indirect allowed transition, or indirect forbidden transition). The optical E_g of a sample can be obtained by intercepting the linear extrapolation of $(\alpha h\nu)^{1/n}$ with the photon energy $h\nu$ axis. Such a plot of the dependence of $(\alpha h\nu)^{1/n}$ on $h\nu$ is generally referred to as a Tauc plot. For highly light scattering and absorbing materials, the α in eqn (1) can be simply approximated from the sample's diffuse reflectance *via* the Kubelka–Munk function:[5]

$$F(R) = \frac{(1-R)^2}{2R} \tag{2}$$

As a result, one of the most general forms of the Tauc plot is with $(F(R)h\nu)^{1/n}$ as the vertical axis and $h\nu$ as the horizontal axis. It should be noted that the E_g value obtained *via* UV-vis spectral analysis strongly depends on the optical electronic transition, the equation used for the graphic representation, and the extrapolation method.
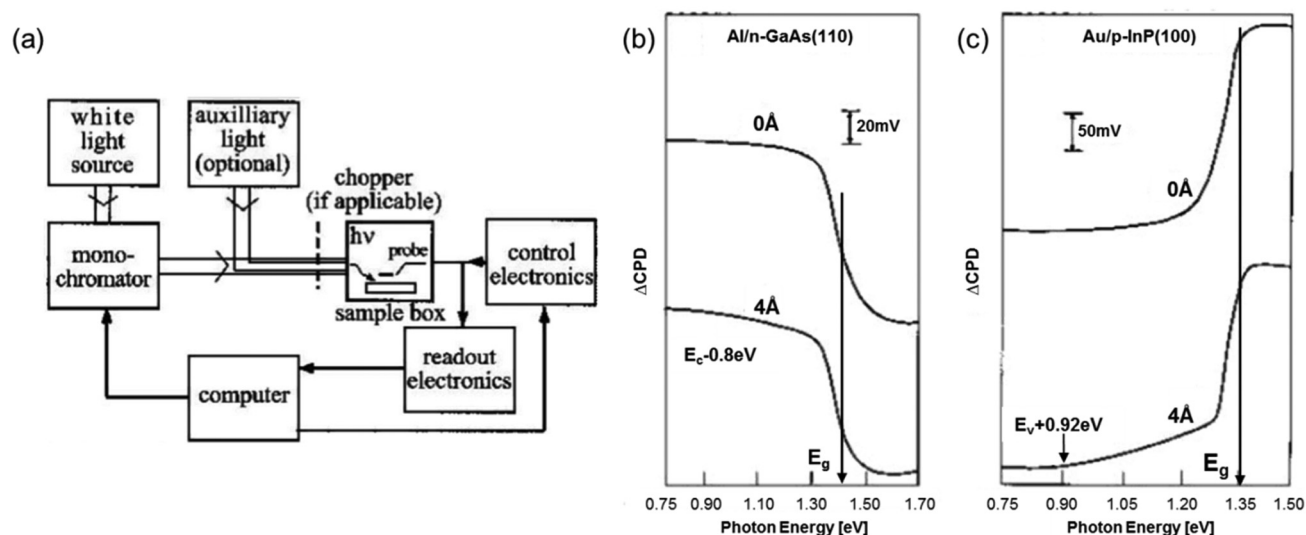
This journal is © The Royal Society of Chemistry 2019

Chem. Soc. Rev., 2019, **48**, 1255–1271 | **1257**

Fig. 3 (a) Schematic of a standard SPS configuration. SPS spectra of (b) n-type GaAs (110) surface and (c) p-type InP (100) surface; the top and bottom curves represent the UHV cleaved surface and the surface with an overlayer of Al or Au, respectively. (a and b) Reproduced from ref. 6 with permission from John Wiley & Sons, Ltd, copyright 2001.

Another optical tool that naturally complements UV-vis diffuse reflectance spectroscopy is the surface photovoltage spectroscopy (SPS). SPS measurements rely on the surface potential changes as a function of the incident photon energy. In principle, redistribution of the excess free carriers generated in a photo-excited semiconductor triggers the surface photovoltage (SPV) signal. Fig. 3a shows the schematic of a typical SPS setup. In short, a metallic box, which serves as a Faraday cage with a dark environment, houses the sample and the probe electrode (*e.g.*, a Kelvin probe or an AFM/STM tip), which are separated at a small distance. The contact potential difference (CPD) between the sample and the probe is then measured, and the change of CPD (ΔCPD) upon illumination is the SPV signal. On the basis of a significant increase in the absorption coefficient near the E_g of most semiconductors with the concomitant substantial change in the SPV signal, the E_g of semiconductors can be estimated simply by identifying the knee (*i.e.*, local maximum) in the SPV curve.[6,7] Examples for the application of this approach are displayed in Fig. 3b and c, in which sharp changes in the slopes of the SPV curves were used to determine the E_g of GaAs and InP. The major limitation of the E_g analyzed using the SPS technique, however, is that it serves only as an approximation due to the relatively broad onset of the SPV signal. This is attributed to the Franz–Keldysh effect and excitation of trapped states (*i.e.*, defect-state-to-band transition) *via* sub-band gap illumination.[6,7]

Following photoexcitation, the excited electrons would take numerous decay pathways, one being radiative recombination accompanied by photon emission, to return to the ground states. This phenomenon is known as photoluminescence (PL). Steady-state PL spectroscopy has thus also been loosely used to define the E_g of semiconductors. The generic configuration of a photoluminescence setup is illustrated in Fig. 4, in which the three primary components are the excitation light

source, the sample cell chamber, and the emitted photon detector. Measurement of the emission spectrum of a sample while it is excited by a monochromatic laser of wavelength energy higher than E_g surveys the permissible electronic transitions from the excited state to the ground state in the material. Proper analysis of the PL spectral distribution therefore enables E_g determination of semiconductors. In spite of that, there are a few key downsides in PL analysis: (1) the necessity to cool the sample to low temperatures (*e.g.*, 77 K or even 4 K) to minimize the competitive non-radiative decay mechanisms that are prevalent at room or higher temperature, thus intensifying the band gap PL emission signal and allowing exploration of the intrinsic optical and electronic properties of the semi-conductor;[8] (2) the presence of Stokes shift, in which the emission energy is generally lower than that of the absorption (the excitation energy) due to the energy loss associated with the vibrational relaxation process as explained in the Perrin–Jablonski diagram, impeding accurate E_g determination.

3. Conduction and valence band edge positions

The (electro)catalytic ability of a semiconductor photocatalyst primarily relies on the electron injection ability of the material at the surface, which is governed by the energetics of the conduction and valence bands. Knowledge on the absolute positions of E_{CB} and E_{VB} band edges is therefore essential to explore the potential applications of the semiconductor of interest. While theoretical calculations based on atomic electro-negativities and density functional theory have been demon-strated to be useful to predict the band edge positions for various semiconductors, reliable experimental approaches are crucial and highly sought after. These approaches are discussed
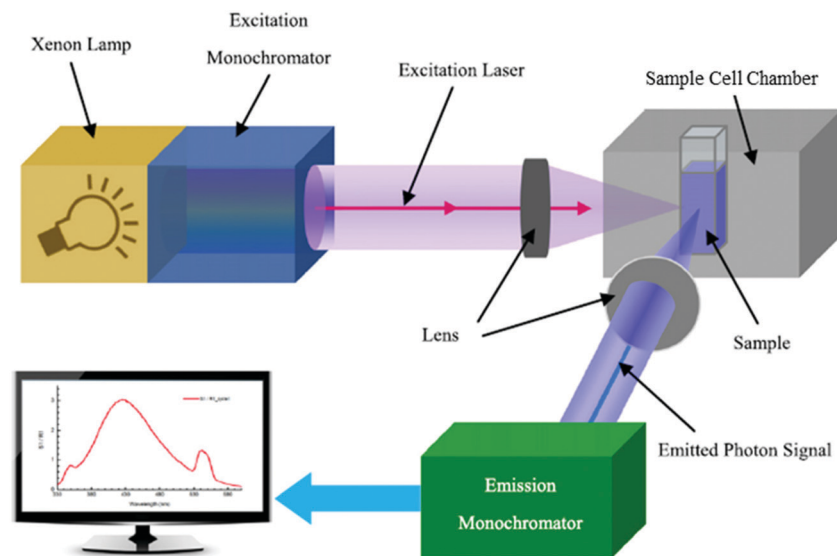
Fig. 4 Schematic diagram of the arrangement of optical components in a typical spectrofluorometer. Reproduced from ref. 9 with permission from the IOP Publishing Ltd, copyright 2014.

in this section. A brief summary of the core energy levels in semiconductors, including Fermi levels, quasi-Fermi levels, vacuum levels, and flatband potentials will first be provided due to their relevance to the determination of E_{CB} and E_{VB} potentials.

The electrochemical potential of electrons in a semiconductor is determined by the Fermi level (E_F). In other words, E_F defines the occupation of the energy levels at thermodynamic equilibrium. Statistically, E_F is the energy level at which the probability to be occupied by an electron is 0.5. Given the typical electron distribution in a semiconductor, E_F lies within the band gap where its position is dependent on the doping concentration and dopant type. For example, the E_F of an n-type semiconductor with electrons as the majority carrier lies close to the conduction band (Fig. 5a). For a p-type semiconductor with holes as the majority carrier, on the other hand, the E_F locates just above the valence band (Fig. 5b). However, the thermodynamic equilibrium of a semiconductor is perturbed under illumination or external applied bias where excess electrons and holes are photogenerated or injected. The non-equilibrium densities of holes in the valence band and electrons in the conduction band are then described by the quasi-Fermi levels. Typically, the quasi-Fermi level for the majority carriers approximates to the equilibrium E_F due to the insignificant increase of the majority carrier density (i.e., $n + \Delta n \simeq n$). Meanwhile, due to the small amount of the minority carriers at equilibrium, it can be greatly escalated (i.e., $p + \Delta p \simeq \Delta p$) which results in a shift of its quasi-Fermi level.[10,11] In other words, E_F acquisition for n-type semiconductors often translates into the determination of the position of the quasi-Fermi level of electrons, whereas it is the quasi-Fermi level of holes for p-type semiconductors. The quasi-Fermi level of the minority carriers can also be estimated, since it is typically assumed that $\Delta n = \Delta p$. For generalization, the technically correct majority carrier quasi-Fermi level will be referred to as E_F hereafter.

Based on the above considerations, determination of E_F corresponds to the conduction band edge position (E_{CB}) for n-type semiconductors (the difference between the two is dependent on the dopant concentration, but it is typically very small for highly doped semiconductors), and it relates to the valence band edge potential (E_{VB}) for p-type semiconductors.

At the surface, the energy of a stationary electron located in close proximity to the semiconductor relates to the vacuum level (E_{VAC}). As a surface property, E_{VAC} is strongly affected by the surface composition or structure. Nevertheless, it has to be differentiated from the vacuum level at infinity ($E_{VAC}(\infty)$), which is defined as the energy of an electron at rest at an infinite distance from the surface. The disparity between E_{VAC} and $E_{VAC}(\infty)$ has been provided by Cahen et al.[12] As opposed to E_{VAC} that is accessible experimentally, $E_{VAC}(\infty)$ has only theoretical implication and therefore is not considered in this review. Instead, E_{VAC} is the pivotal reference level that defines all the other parameters as illustrated in Fig. 5; the energy needed to excite an electron from E_{VB}, E_F, or E_{CB} to E_{VAC} is respectively known as the ionization energy (IE), the work function (ϕ), or the electron affinity (χ). Similar to that of E_{VAC}, all these parameters are surface-related and hence are being defined only at the semiconductor surface.

When a semiconductor is in contact with another phase, the ionic interactions at the interface of the two phases lead to electrostatic adjustments within the material. At the semiconductor/electrolyte interface, in particular, electrons flow from the phase of more negative E_F to the other to attain equilibrium, in which the semiconductor E_F matches the electrolyte $E_{F,redox}$. This causes the formation of a space charge layer (SCL) within the semiconductor phase that is associated with the upward bending of the band edges in the n-type semiconductor (Fig. 5c) and downward band bending in the p-type semiconductor (Fig. 5d). The SCL contributes to an internal electric field in the semiconductor, in which the
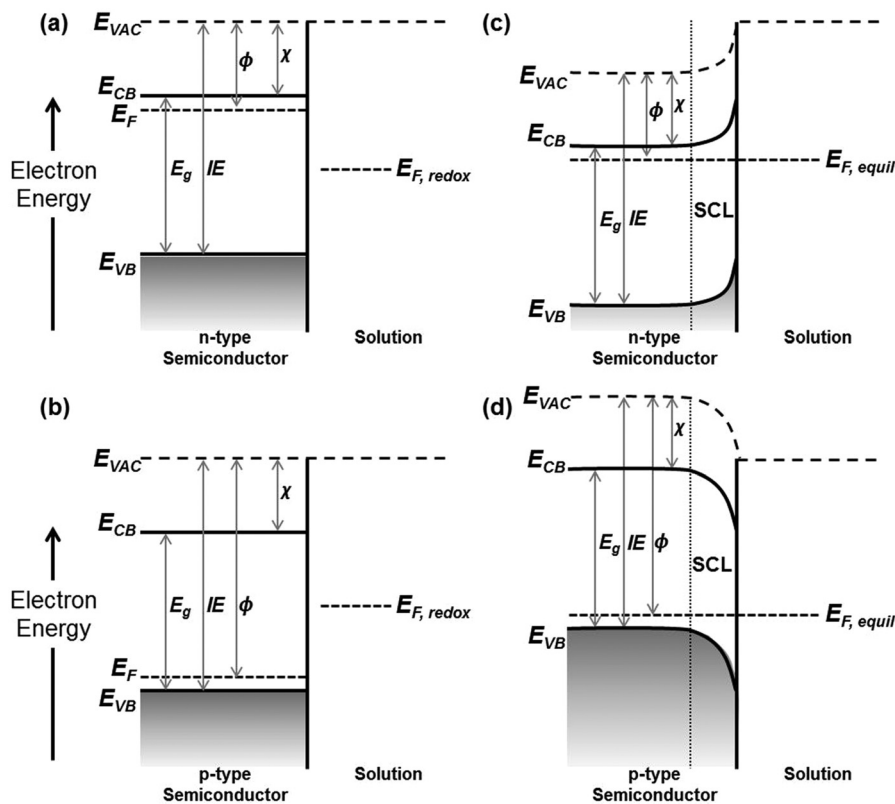
Fig. 5 Energy levels of the semiconductor/electrolyte interface (a and b) before and (c and d) after contact. The semiconductors in (a and c) correspond to an n-type semiconductor, whereas (b and d) relate to a p-type semiconductor. E_{VAC}: vacuum level, E_{CB}: bottom of the conduction band, E_F: Fermi level, E_{VB}: top of the valence band, E_g: band gap, IE: ionization energy, ϕ: work function, χ: electron affinity.

majority carriers are forced away from the semiconductor/electrolyte interface. Such a SCL accounts for one of the three distinct double layers, in addition to the Helmholtz layer and Gouy–Chapman layer that are typically present at the semiconductor/electrolyte interface.[10] The magnitude and direction of band bending can simply be adjusted by an externally applied potential. Another important concept to be introduced is the flatband potential (E_{FB}), which is the applied bias that diminishes the band bending in a semiconductor that is in contact with the electrolyte. The E_{FB} therefore carries fundamental significance as it corresponds to the E_F of the semiconductor.

Note that the preceding discussion mainly refers to ideal behavior of semiconductors in the absence of surface states for simple presentation of the fundamental and theoretical energetics at the semiconductor/electrolyte interface. The non-ideal behavior of semiconductors can be found elsewhere.[10,11]

One commonly employed experimental technique to determine band edge positions based on E_{FB} measurement is *via* (photo)-electrochemical methods described as follows:

(1) Capacitance measurement according to the Mott–Schottky function:

$$\frac{1}{C^2} = \frac{2}{A^2 \varepsilon \varepsilon_0 q N_D}\left(E - E_{FB} - \frac{k_B T}{q}\right) \qquad (3)$$

where C is the capacitance in the SCL, A is the semiconductor/electrolyte interfacial area, ε is the dielectric constant of the semiconductor, ε_0 is the permittivity of free space, q is the electronic charge, N_D is the donor density, E is the applied potential, k_B is Boltzmann's constant, and T is the absolute temperature. A plot of $1/C^2$ against E permits E_{FB} and N_D to be respectively determined from the x-axis intercept and the slope of the linear region;

(2) Photocurrent onset examination, in which the E_F of the semiconductor is altered using an externally applied potential to show the photocurrent dependence on the potential. The potential value at which the photocurrent appears or vanishes (depending on the potential sweeping direction) corresponds to the E_{FB} of the semiconductor;

(3) Open-circuit photovoltage measurement, in which the electrode open-circuit potential is measured as a function of the illumination intensity. At satisfactorily high intensity, the open-circuit potential becomes constant and can be taken as the E_{FB} of the semiconductor.

A comprehensive discussion on each of these electrochemical-related approaches can be found in the review provided by Beranek.[11] Although the review mainly reports the use of the (photo)electrochemical methods on n-type TiO$_2$, they can also be effectually implemented for examination of the E_{FB} for other semiconductors, including p-type materials. However, it must be noted that the obtained results correspond to the E_{CB} for an n-type semiconductor, while it is the E_{VB} for a p-type semiconductor. When one of the band edge potentials is defined,

1260 | *Chem. Soc. Rev.*, 2019, **48**, 1255–1271

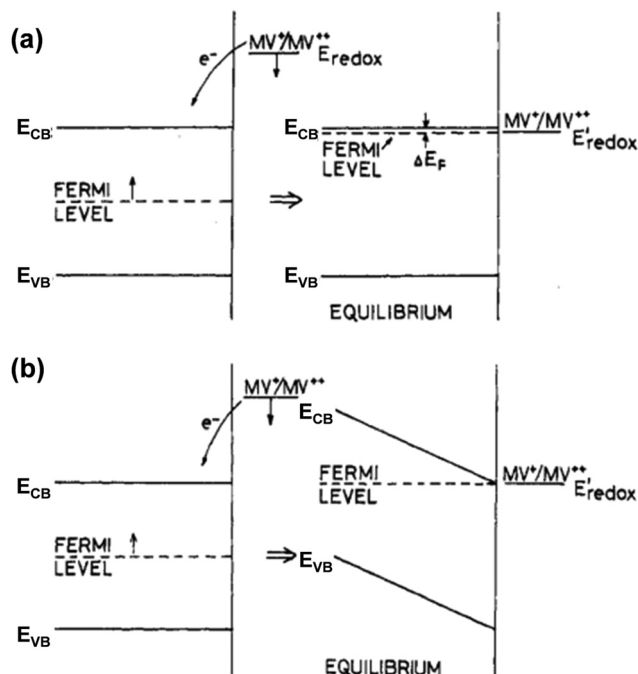This journal is © The Royal Society of Chemistry 2019

(a)

(b)

Fig. 6 Energy level diagrams of a semiconductor before and after charge equilibration with the MV^{2+}/MV^+ redox couple, in which the semiconductor's Fermi level (E_F) is more positive than the redox potential of MV^{2+}/MV^+. The electron injection from MV^{2+}/MV^+ into the semiconductor leads to downward shifting of E_{redox} to more positive values; meanwhile (a) E_F could be shifted upwards such that it approaches E_{CB} or (b) SCL could be formed on the semiconductor surface due to the band bending. In both cases (a and b), $E_{redox} = E_F$ at equilibrium. Reproduced from ref. 14 with permission from the American Chemical Society, copyright 1984.

the other can be reasonably deduced based on the E_g value (*i.e.*, $E_g = E_{VB} - E_{CB}$) analyzed *via* the methods delineated in Section 2.

In addition to the aforementioned (photo)electrochemical methods, the E_{FB} of semiconductors, particularly in the particle form, can also be effectively acquired by exploiting the equilibrium concentration of an appropriate redox couple (Red/Ox; *e.g.*, MV^{2+}/MV^+, Cu^{2+}/Cu^+, or $C_{60}/C_{60}^{\bullet-}$) upon charge equilibration with the semiconductor.[13,14] One example for such a phenomenon is schematically illustrated in Fig. 6. In the presence of the MV^+ species that have a redox potential more negative than the semiconductor E_F, MV^+ is favorably oxidized to form MV^{2+} ($MV^+ \rightarrow MV^{2+} + e^-$), and the resulting electrons are then injected into the conduction band of the semiconductor. The electron injection can either raise the Fermi level of the semiconductor to approach the E_{CB} (Fig. 6a) or develop a SCL on the semiconductor surface associated with band bending (Fig. 6b), leading to equilibration between the E_F of the semiconductor and the redox potential of the redox couple. This equilibrium potential is therefore identified as the E_{FB} of the semiconductor, which can be calculated according to the Nernst equation:[13]

$$E_F = E_{FB} = E^{\circ}_{(Red/Ox)} + 0.059 \log \frac{[Red]_{eq}}{[Ox]} \quad (4)$$

Another tool reported to be prompt in obtaining the E_{FB} of semiconductors is the electrolyte electroreflectance (EER) technique. This technique involves modulating the electric field in the SCL in the semiconductor by ac voltage and determining the resulting changes in reflectance ($\Delta R/R$). Typically, the EER $\Delta R/R$ signal would change sign (*i.e.*, reversal of spectrum shape) when the semiconducting electrode is polarized from depletion into accumulation. The potential at which the change of sign of $\Delta R/R$ occurs corresponds to the E_{FB} of the semiconductor. Taking the EER spectra of $CuInSe_2$ polycrystalline electrodes as an example (Fig. 7a), the reversal of the signal between the applied biases V_{dc} of -0.8 and -1.0 V infers that the E_{FB} of the material locates at $-1.0 < V_{dc} < -0.8$ V *vs.* SCE.[15] Salvador and co-workers proposed that an accurate value of the E_{FB} can be evaluated by monitoring the amplitude and phase changes of the EER signal (*i.e.*, $|\Delta R/R|$ and ϕ, respectively) at a fixed wavelength while sweeping the applied potential V_{dc}; the potential at which $|\Delta R/R|$ reaches a zero minimum and ϕ experiences 180° shift is therefore the E_{FB}. Using this approach, the E_{FB} of the $CuInSe_2$ electrode was found to be -0.87 ± 0.01 V *vs.* SCE, as shown in Fig. 7b.[15] With a similar concept, electrolyte electroabsorption (EEA) measurements can also be applied to determine the E_{FB} value for transparent and thin photoelectrodes.

Instead of measuring E_F or E_{FB}, the E_{VB} of semiconductors can be directly measured using spectroscopic techniques such as X-ray photoelectron spectroscopy (XPS) and ultraviolet photoelectron spectroscopy (UPS). Typically, the E_{VB} is related to the leading edge (close to 0 eV binding energy) of the photoemission spectra. There are two methods reported to evaluate the E_{VB} value from the XPS valence band spectrum:

(1) Kraut method, a hybrid experimental–theoretical approach, in which the leading edge of the XPS spectrum is modelled and fitted by a Gaussian broadened theoretical valence band density of states;[16]

(2) Linear method, in which the point of intersection between the regression line fitted to the linear region of the XPS valence band leading edge and the background line is employed[17]

While method (1) falls short of precise prediction of the valence band leading edge shapes of oxide semiconductors, the E_{VB} values predicted using method (2) were demonstrated to be comparable to that acquired by the UPS leading edge spectra, at which the E_{VB} is identified as the energy where the intensity approaches zero.[17] Despite that, UPS surpasses XPS in studying the valence band fine structures since the former employs lower energy photons as the excitation source and thus it has higher sensitivity in the valence band region. Not only does UPS provide determination of E_{VB} relative to E_F (as that of XPS valence band measurement since both the UPS and XPS spectra are generally calibrated such that E_F is located at binding energy 0 eV), it also allows direct acquisition of the E_{VAC} of the sample.

The photoemission process in relation to UPS measurement was detailed by Cahen and Kahn,[12] as shown in Fig. 8a. The secondary electron cut-off (as specified in Fig. 8b) relates to the minimum energy (E_k^{min}, as indicated in Fig. 8a) an electron can
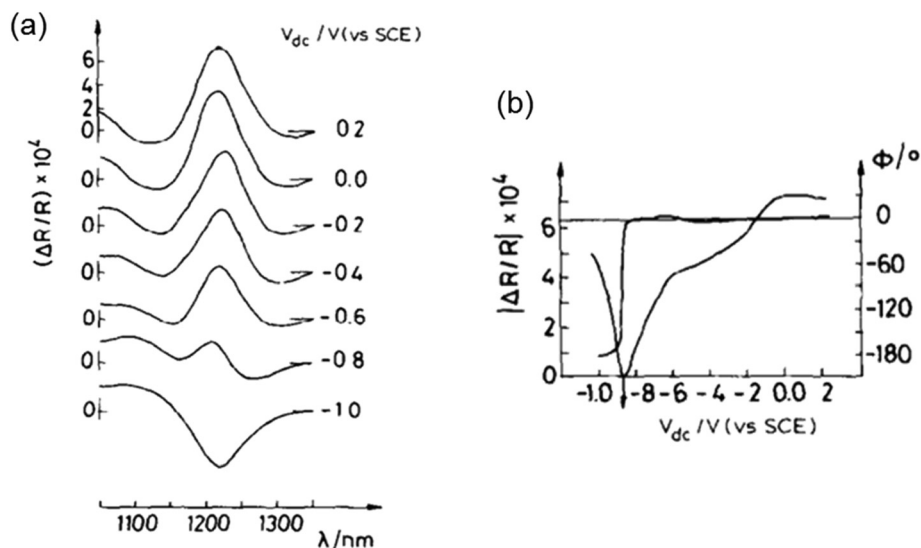
This journal is © The Royal Society of Chemistry 2019

Chem. Soc. Rev., 2019, **48**, 1255–1271 | **1261**

Fig. 7 (a) EER spectra of CuInSe$_2$ at different applied V_{dc} biases. (b) Dependence of the EER signal phase (ϕ) and amplitude ($|\Delta R/R|$) on the applied bias V_{dc}, measured at λ = 1220 nm. Figure a and b: reproduced from ref. 15 with permission from Elsevier B.V., copyright 1988.

have to escape from the solid to arrive at E_{VAC}. It is essential to pinpoint the secondary cut-off or E_k^{min} position in the UPS spectrum because the location of E_{VAC} with respect to the spectrum is equivalent to the translation of the cut-off or E_k^{min} position by one photon energy $h\nu$. The UPS spectra of Pt/TaON and Au obtained from an excitation energy $h\nu$ of 21.2 eV are illustrated in Fig. 8b,[18] indicating the standard UPS spectral distribution in relation to the E_{VB}, E_F, and E_{VAC} energy levels. Following the identification of E_{VB}, E_F, and E_{VAC} in the UPS spectrum, the ionization energy (IE) and work function (ϕ) of the sample can then be calculated to deduce the absolute electron potentials of E_{VB} and E_F, respectively. In particular, ϕ can be calculated according to eqn (5),[12] which

is identical to subtracting the energy difference between the E_F and the cut-off from the incident photon energy.

$$\phi = h\nu - E_k^{max} + E_k^{min} \tag{5}$$

Clearly, UPS enables the most detailed characterization of the electronic band structures of a semiconductor, particularly when it is used in conjunction with another optical tool for E_g determination to compute E_{CB}.

The major difference in the energetic levels analyzed *via* the spectroscopic techniques and the (photo)electrochemical approaches is that the potentials are generally measured with respect to the vacuum level (*i.e.*, absolute electron potential, E_{abs})
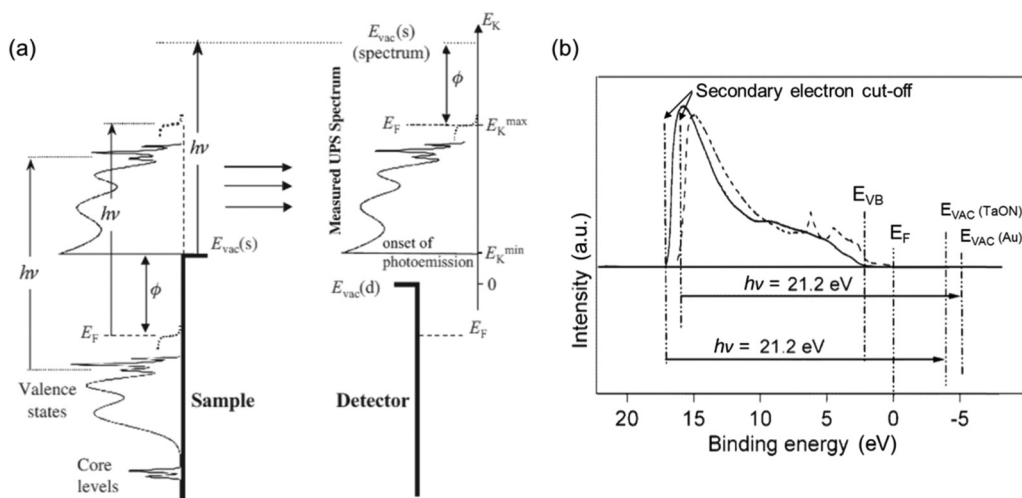

Fig. 8 (a) Schematic illustrates the generic photoemission process and the resulting UPS spectrum of a semiconductor in the scale of kinetic energy E_k. Reproduced from ref. 12 with permission from WILEY-VCH Verlag GmbH & Co. KGaA, Weinheim, copyright 2003. (b) The UPS spectra of Pt/TaON (solid line) and Au deposited on Pt/TaON (dashed line), indicating the relevant positions of E_{VB}, E_F, and E_{VAC} energetic levels with respect to the spectra. Reproduced from ref. 18 with permission from the American Chemical Society, copyright 2003.

in the former, but with respect to the normal hydrogen electrode NHE (*i.e.*, standard electrode potential, E°, where $E^\circ(\text{H}^+/\text{H}_2) = 0$ V) in the latter. However, the relationship between the E_{abs} and E° has been established (eqn (6)),[19] facilitating correlation of the experimental data attained from the two methods.

$$E_{\text{abs}} = -E^\circ - 4.44 \qquad (6)$$

It should be noted that there remains an uncertainty as to which pH value should the spectroscopic data be correlated with.[18] This is because the potentials of the surface-related band edges (*i.e.*, E_{CB} and E_{VB}) and E_{F} acquired *via* the (photo)-electrochemical methods in an aqueous electrolyte are pH sensitive, particularly for oxide semiconductors, attributed to the surface adsorption of protons and hydroxyl groups.

4. Charge carrier dynamics

In addition to the optical properties and the energetic levels described in the previous sections, the charge carrier properties of the semiconductor photo(electro)catalyst are also essential. In other words, the charge carrier dynamics need to be well understood in order to know the extent to which the photo-catalytic or photoelectrochemical properties of the semiconductor can be improved. Both bulk and surface carrier dynamics are important; several measurement techniques and procedures reported for both are discussed here. Note that although several examples shown here are based on photoelectrode systems, the measurements can also be adapted for particle-based systems by immobilizing the particles on a suitable substrate. The obtained properties are often transferable.

Upon photoexcitation, charge carriers that are generated in the bulk of the semiconductor photoelectrodes need to travel to the interfaces (*i.e.*, semiconductor/electrolyte and semiconductor/substrate interfaces). In many cases, especially in metal oxide semiconductors, the optical penetration depth of a semi-conductor is much larger than the extent of the SCL (*i.e.*, part of the semiconductor where an electric field is present, as explained in Section 3). Therefore, carrier transport occurs predominantly through a diffusion process rather than drift. A critical property of a semiconductor is the minority carrier diffusion length (L_{D}), which is the distance that minority carriers can travel before they recombine with the majority carriers (either direct band-to-band or through defect-mediated states). One way to determine L_{D} is by performing wavelength-dependent photovoltage or photocurrent measurements. For example, the photovoltage of the sample can be measured using the SPS technique, which has been previously touched upon in Section 2. For an n-type semiconductor with a depletion layer width (w_{d}) much smaller than both the absorption length and the L_{D}, the excess minority carrier (δp) can be expressed in the following form:[6,7]

$$\delta p = \frac{\alpha L_{\text{D}}}{1 + \alpha L_{\text{D}}} \times \frac{1}{S + D/L_{\text{D}}} \times I \qquad (7)$$

where α is the absorption coefficient, D is the diffusion constant of minority carriers, S is the effective drift velocity, and I is the

photon flux intensity. Typically, the SPV signal can be assumed to have a monotonic dependence on δp.[6,7] For a constant SPV signal, and considering that S and D are constants, eqn (7) can be re-written as follows:

$$I = C \times (\alpha^{-1} + L_{\text{D}}) \qquad (8)$$

where C is a constant. eqn (8) implies that if the intensity used to obtain the constant SPV signal (I) is plotted as a function of α^{-1} for various wavelengths, the x-axis intercept of this plot is equal to $-L_{\text{D}}$. If not already known, a separate optical UV-vis measurement needs to be done to determine α (refer to Section 2). This method of extracting L_{D} was first proposed by Goodman and is usually known as the 'constant SPV' approach. For example, Li showed the extraction of L_{D} for InP samples using this approach, as shown in Fig. 9a.[20] It can be seen that the approach is not affected by the pre-selected constant SPV signal; a diffusion length of ~1.3 µm was obtained for InP. This method has also been used to determine the L_{D} for other materials, *e.g.* Si, GaN, CdTe, and metal halide perovskites.[21,22]

In addition to SPS, other spectral approaches have also been performed to extract L_{D} in the form of electron-beam induced current (EBIC) and internal quantum efficiency (IQE) measure-ments. The EBIC-based method typically requires the for-mation of a Schottky-junction using a metal layer and the semiconductor of interest. A focused electron beam then bom-bards the sample, and the collected current density (J) is measured. The collection efficiency (e) can then be determined using the following relationship:

$$e = \frac{|J|}{qG_0} \qquad (9)$$

where G_0 is the total carrier generation rate that is related to the incident electron-beam voltage. By measuring e as a function of the incident beam voltage, the resulting plot can be fitted in order to obtain the value of L_{D}.[23] Fig. 9b shows the example of such a plot for n-type GaAs. However, EBIC is typically a destructive technique, and the analysis requires that the w_{d} of the sample is known. Alternatively, one can also measure the IQE of the sample as a function of wavelength and applied potentials. Separately, capacitance–voltage (CV) measurements of the sample are needed to establish the dependence of the w_{d} as a function of applied potentials. Gärtner approximation, which provides the relationship between the photo-generated current, w_{d}, and L_{D}, can then be used:[24]

$$\text{IQE} = 1 - \frac{\exp(-\alpha w_{\text{d}})}{1 + \alpha L_{\text{D}}} \qquad (10)$$

If α is known, this can be used to determine L_{D}; otherwise, the array of IQE data as a function of wavelength and applied potentials need to be fitted with eqn (10) to extract a single L_{D} value and α for each wavelength.

Another somewhat innovative approach was recently reported by Pala *et al.* using wedge-shaped semiconductor photoelectrodes.[25] They showed that for a sample with a thickness (w) much larger than w_{d}, the photocurrent (J) is approximated as a

This journal is © The Royal Society of Chemistry 2019

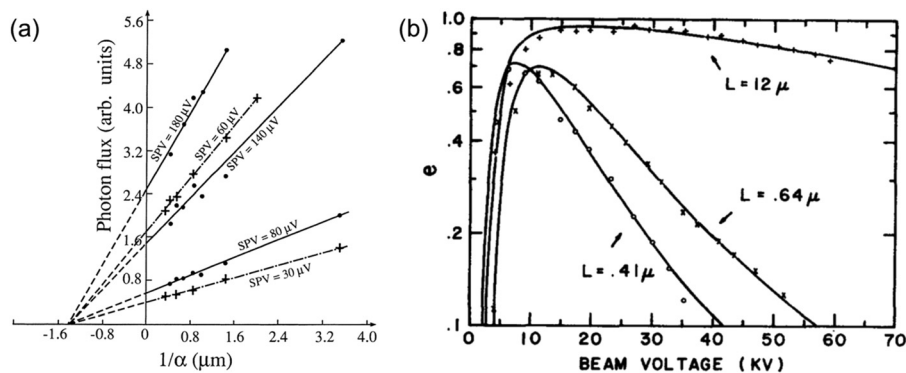*Chem. Soc. Rev.*, 2019, **48**, 1255–1271 | **1263**

Fig. 9 (a) Determination of the diffusion length of (100) InP samples from the intercepts of the photon flux *vs.* the inverse absorption coefficient ($1/\alpha$) for several surface photovoltage (SPV) values. Reproduced from ref. 20 with permission from the AIP Publishing, copyright 1976. (b) EBIC collection efficiency (*e*) *vs.* beam voltage for Au-GaAs (n-type) Schottky barrier diodes. The GaAs samples have different carrier concentrations: 6.8×10^{15} cm^{-3} ("+"), 1.3×10^{17} cm^{-3} ("×"), and 1.1×10^{18} cm^{-3} ("○"). The diffusion lengths for each sample were obtained by fitting the data points (solid lines) with the model reported by Wu and Wittry.[23] Figure a and b: reproduced from ref. 23 with permission from the AIP Publishing, copyright 1978.

constant factor multiplied by the reciprocal exponential of w/L_D (*i.e.*, $J \propto \exp(-w/L_D)$). Using a wedge-shaped semiconductor photoelectrode deposited on a transparent substrate (Fig. 10a), they measured the back-side illuminated photocurrents at various points of the electrode (*i.e.*, different thicknesses). Plotting the natural logarithm of photocurrents as a function of thickness therefore yields a straight line with a slope of $-1/L_D$. Examples of L_D determination in Si and BiVO$_4$ wedge photoelectrodes are shown in Fig. 10b and c, respectively. At lower thicknesses, this approximation does not hold (since w_d is in the range of w); but the approach was successfully demonstrated for higher thicknesses. It should also be noted that the method should not be wavelength-dependent, as long as the absorption length is much shorter than the diffusion length (see Fig. 10c). Finally, although it is definitely much more efficient using the wedge geometry, the same method can be performed using multiple samples with

different thicknesses if deposition of wedge photoelectrodes is not possible.

Instead of determining L_D directly, one can also calculate L_D from the carrier mobility (μ) and lifetime (τ) of the sample. The following expressions can be used:

$$D = \frac{\mu k T}{q} \tag{11}$$

$$L_D = \sqrt{D\tau} \tag{12}$$

where k is the Boltzmann constant, T is the temperature and q is the elementary charge. While τ is usually determined using time-resolved measurements (*e.g.*, by fitting the decay of the time-resolved photoluminescence (TRPL) signal), μ can be determined by measuring the conductivity of the sample (*i.e.*, measuring a potential drop as a result of passing current through a well-defined sample geometry (four-point collinear
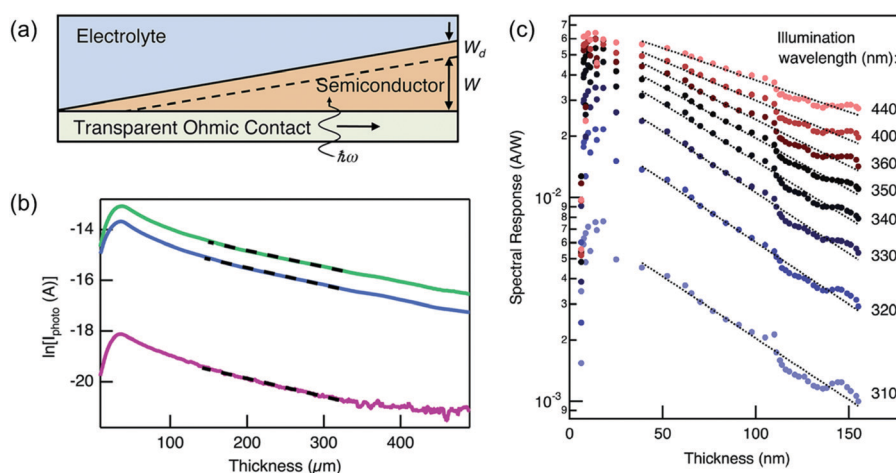

Fig. 10 (a) Schematic of the wedge-shaped sample geometry used in the measurement of L_D by Pala *et al.*[25] (b) Natural logarithm of photocurrent *vs.* thickness of a Si wedge illuminated with (top to bottom) 500, 455, and 365 nm light. The L_D was calculated to be 168 µm by linear fitting of the data (dashed lines). (c) Similar data as in (b) but for a BiVO$_4$ wedge. The slope is not constant when the illumination wavelength is larger than 340 nm because the absorption length is larger than the L_D. A L_D of 75 nm was calculated by linear fitting the data at wavelengths of 310, 320, and 330 nm. Figure a–c: reproduced from ref. 25 with permission from The Royal Society of Chemistry, copyright 2014.

1264 | *Chem. Soc. Rev.*, 2019, **48**, 1255–1271

This journal is © The Royal Society of Chemistry 2019

or van der Pauw)).[26] Conductivity (σ) is related to μ through the following expression (for an n-type semiconductor):

$$\sigma = qn\mu \tag{13}$$

Here, n is the carrier concentration, which is typically obtained from other measurements (*e.g.*, Mott–Schottky, see Section 3). Alternatively, Hall effect measurements are widely used to determine the μ of a semiconductor. The measurement is similar to the standard conductivity measurements (van der Pauw geometry is often used), but with the addition of a magnetic field. In short, it measures the deflection of charge carriers in the presence of a magnetic field perpendicular to the flow of the carriers.[26] Using experimentally measured Hall voltage (V_H), applied current (i), applied magnetic field (B), and sample thickness (w), the Hall coefficient (R_H) can be calculated:

$$R_H = \frac{V_H w}{iB} \tag{14}$$

Hall mobility (μ_H) is then calculated using the σ of the sample (either known or measured):

$$\mu_H = \sigma R_H \tag{15}$$

The methods described in the previous paragraph to determine τ and μ, however, have certain issues and limitations. (1) First, determining τ through TRPL requires that the decay mechanism is radiative recombination, thus generating luminescence signals. However, carriers may also decay through non-radiative pathways, which are undetected by TRPL measurements. (2) The μ values obtained, either the drift mobility from conductivity measurements or the Hall mobility from Hall measurements, are the majority carrier mobility. Methods using photo-Hall measurements to determine both the majority and minority carrier mobility have been recently developed,[27] but these methods are not yet widely used. (3) In addition, many of the semiconductor photoelectrodes of interest for solar water splitting have very high resistivity; measuring their σ is therefore not trivial. Moreover, carrier transport in most of these semiconductors (especially metal oxides) occurs *via* a small polaron hopping mechanism,[26,28] instead of the band transport mechanism. This has been shown to result in anomalies and further complications when analyzing the Hall measurement results.[29]

Time-resolved photoconductivity measurements using microwave probe signals have also been used in order to determine both μ and τ. In time-resolved microwave conductivity (TRMC), the sample is placed in a microwave cell, and it is subjected simultaneously to a short (typically in the range of a few nanoseconds) laser pulse radiation and a microwave probe. The setup is described in detail elsewhere,[30] and a typical schematic of the setup is shown in Fig. 11a. Since microwave interacts with mobile carriers, the photoexcitation by the laser pulse creates a change in the reflected power of the microwave. The normalized change in the microwave power reflected by the cavity upon sample excitation ($\Delta P/P$) can be correlated with the photoinduced change in the conductance of the sample (ΔG), by the following:

$$\frac{\Delta P}{P} = -K\Delta G \tag{16}$$

where K is the sensitivity factor derived from the resonance characteristics of the cavity and the dielectric properties of the sample. From this ΔG value, the product of the charge carrier generation yield (ϕ, typically assumed to be 1 for inorganic
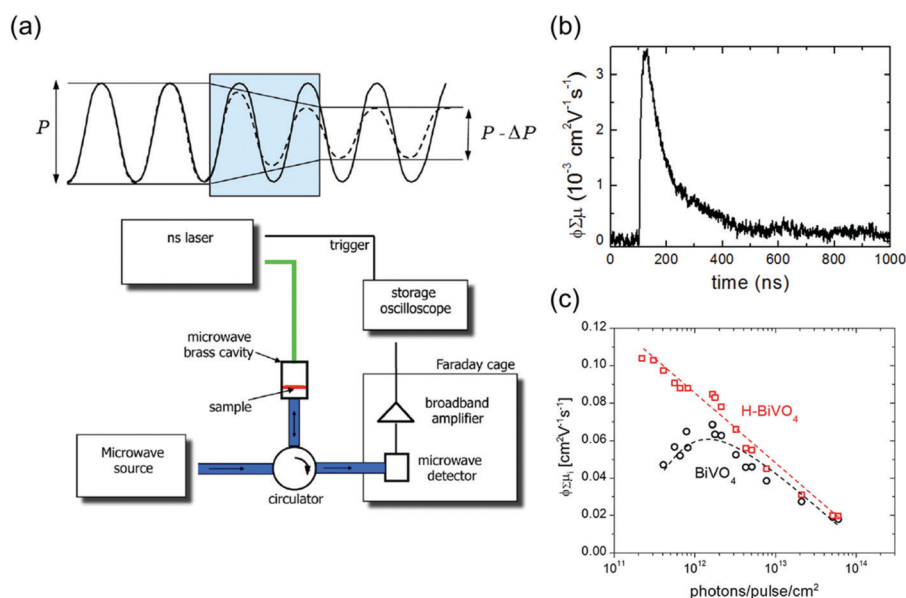
Fig. 11 (a) (top) Illustration of the attenuation of microwaves due to propagation through a weakly conducting medium. (bottom) Schematic representation of a typical TRMC setup. Reproduced from ref. 30 with permission from the American Chemical Society, copyright 2013. (b) TRMC signal ($\phi\Sigma\mu$ *vs.* time) measured for undoped spray-pyrolyzed BiVO$_4$. Reproduced from ref. 31 with permission from the American Chemical Society, copyright 2013. (c) Maximum observed TRMC signals (maximum $\phi\Sigma\mu$) as a function of incident photons for pristine and hydrogen-treated BiVO$_4$. Reproduced from ref. 32 with permission from WILEY-VCH Verlag GmbH & Co. KGaA, Weinheim, copyright 2017.

This journal is © The Royal Society of Chemistry 2019

Chem. Soc. Rev., 2019, **48**, 1255–1271 | **1265**

semiconductors with low exciton binding energy) and the sum of electron and hole mobilities ($\Sigma\mu$) can be obtained according to the following:

$$\phi\Sigma\mu = \frac{\Delta G}{I_0 \beta q F_A} \qquad (17)$$

where I_0 is the incident laser intensity per pulse per unit area, q is the elementary charge, β is the ratio between the inner broad and narrow dimensions of the waveguide, and F_A is the fraction of incident photons absorbed within the sample.

A typical $\phi\Sigma\mu$ plot as a function of time (here taken from a BiVO$_4$ photoanode as an example) is shown in Fig. 11b. From the peak of the plot (i.e., the maximum $\phi\Sigma\mu$), the μ value is typically obtained. The decay of the curve is usually fitted with a single-/multi-exponential or a power-law function, from which τ can be determined. It should be noted that microwave is sensitive to all types of carriers, i.e., specific electron and hole mobility values cannot be distinguished. If the electron and hole effective masses in the sample are known (e.g., from DFT calculation), each mobility value can be calculated, but this is again under the assumption that both electron and hole have the same carrier scattering time. Nevertheless, the results obtained from TRMC can serve as a good estimate for the μ and τ—and therefore the L_D—of a semiconducting photoelectrode.

Further information that can be obtained from TRMC is whether trap states are present and trap-assisted recombination affects the carrier transport in a photoelectrode. This is done by performing TRMC measurement at various laser pulse intensities and plotting the mobility values (i.e., the maximum $\phi\Sigma\mu$) vs. the pulse intensities (i.e., I_0). When trap states are present, the mobility first increases with increasing pulse intensity until it reaches a maximum; beyond this point, it again decreases with higher pulse intensity. This has been attributed to the competition between trap filling and higher order recombination.[30,32] Prior to the maximum point, the concentration of trap states is higher than the number of absorbed photons. The mobility, therefore, increases until the entire trap states are filled, and it reaches a maximum. Beyond that, the mobility decreases due to fast non-geminate higher order recombination during the laser pulse. On the other hand, when no trap states are present, the mobility is expected to monotonically decrease with increasing pulse intensity, due to the same higher order recombination, i.e., no maximum is observed. Fig. 11c shows an example from a recent result of a pristine and a hydrogenated BiVO$_4$ photoanode.[32] A clear maximum is observed for the pristine photoanode, indicating the presence of trap states, whereas the hydrogenated photoanode shows only a monotonic decrease of mobility with laser pulse intensity. The density of trap states can also be estimated by dividing the laser pulse intensity at which the maximum point is located with the thickness of the photoanode. Using the example from Fig. 11c, since the maximum point is located at $\sim 2 \times 10^{12}$ pulse^{-1} cm^{-2} and the thickness of the photoanode is ~ 200 nm, the density of trap states is estimated to be $\sim 10^{17}$ cm^3.

Although TRMC provides advantages that it directly measures the actual photoconductivity, and it is also applicable to indirect-gap semiconductors (unlike luminescence), several disadvantages remain. First, as already mentioned above, it does not allow for the differentiation between the majority and minority carriers. An approximation can be made, but this has to be done with extra care and assumptions. Second, the sample needs to be deposited on a non-conductive substrate (e.g., quartz, sapphire). This is of course different than the operando condition of the photoelectrode during the photo-electrochemical measurements. External potentials cannot be applied, and deposition on conducting (e.g., FTO-coated glass) and non-conducting substrates may result in different growth and properties of the sample. Several groups have attempted to perform in situ microwave reflection measurements in a photo-electrochemical cell using a conducting substrate that is selectively etched,[33] but the sensitivity of the measurement is much lower as compared to when a cavity cell is used. A combination of the TRMC results and other techniques, as described earlier, is therefore still needed to provide a complete carrier dynamics picture of a photoelectrode.

Once the charge carriers (electrons or holes) reach the interface, they can either recombine or transfer to the electron acceptor/donor in the electrolyte (e.g., water reduction/oxidation). Apart from the bulk charge carrier properties such as L_D, μ, and τ that have hitherto been discussed, the rate of the interfacial processes is also of interest and can be determined using time-resolved or frequency-resolved techniques. Examples of time-resolved techniques are transient absorption spectroscopy (TAS) and photo-induced absorption (PIA) spectroscopy. Both techniques use an optical illumination (pump) to generate charge carriers in the semiconductor and an additional optical illumination (probe) to monitor the fate of these charge carriers. The charge carriers therefore need to show distinct optical signatures in the measured spectra. This is not always the case, but measurements in the presence of hole and electron scavengers in the electrolyte can help identify these signatures.[34] In TAS, both the pump and probe are typically short laser pulses (fs–ns) which are separated by a certain delay. By varying the delay between the pump and the probe light, the optical absorption change (ΔA) in the sample can be measured as a function of time. Since water oxidation and reduction are typically slow processes, it is therefore important to be able to measure with a relatively long delay (µs–s). Based on the decay of the ΔA, the lifetime of the charge carriers accumulating at the interface and the rate constant for water oxidation or reduction can then be determined.[34] PIA, on the other hand, usually uses much longer optical pulses (seconds) with an LED as the pump, while the probe is continuous illumination (e.g., Xe lamp with a monochromator). Fig. 12a shows the schematic of a typical PIA setup. The PIA signal, ΔA, as well as the photocurrent of the sample are then monitored as the LED turns on and off. Fig. 12b and c show the PIA signals and photocurrents from a report on a BiVO$_4$ photoanode by Ma et al.[35] In that study, they were able to quantify the amount of surface hole density by correlating the PIA signals and the photocurrent transients. Using a simple kinetic model,[35]

1266 | Chem. Soc. Rev., 2019, 48, 1255–1271

This journal is © The Royal Society of Chemistry 2019

the relationship between the photocurrent and the surface hole density could be derived, and the rate constant for water oxidation as well as the reaction order (α) were determined. It was found that water oxidation on the $BiVO_4$ photoanode undergoes a transition from first to third order reaction at a surface hole density of 1 nm^{-2} (Fig. 12d).

Instead of time-resolved measurements, the charge carrier dynamics at the semiconductor/electrolyte interface can also be investigated using frequency-resolved techniques. An example is intensity modulated photocurrent spectroscopy (IMPS). Here, the sample is subjected to a small-amplitude modulated illumination (e.g., using LED), which results in a modulated photocurrent. A schematic of the setup is shown in Fig. 13a. The frequency of the resulting modulated photocurrent is the same as that of the illumination, but the magnitude and phase are generally different. This complex photocurrent response consists of the sum of the minority and majority carrier currents. By scanning the frequency during the measurements, a Nyquist plot can be constructed showing the real and imaginary parts of the photocurrent. An example is shown in Fig. 13b for an n-type semiconductor (i.e., photoanode). The lower quadrant semicircle at higher frequencies represents the attenuation by the total cell series resistance (R) and cell capacitance (C_{cell}).[36,37] The cell capacitance is a combination of the space charge and Helmholtz capacitances (C_{SC} and C_H), but C_H can usually be neglected for materials with moderate charge carrier density. The upper quadrant semicircle at lower frequencies is usually called the recombination semicircle. This is based on a simplified model, described in detail in the study

by Peter et al.,[36,37] which assigns this semicircle to the competition between charge transfer (i.e., hole injection into the electrolyte for a photoanode and electron injection for a photocathode) and charge recombination at the semiconductor/electrolyte interface. The semicircle reaches a maximum when the frequency matches the characteristic relaxation constant of the system:

$$\omega_{max} = k_{tr} + k_{rec} \qquad (18)$$

where k_{tr} is the reaction rate constant for charge transfer, and k_{rec} is the reaction rate constant for charge recombination. At the high frequency intercept with the real photocurrent axis, the fast modulation freezes the charge recombination; normalizing the photocurrent at this point against the hole current for a photoanode (j_{photo}/j_h) therefore gives a value of 1. The fraction of holes at the surface that is injected into the electrolyte can be determined from the low frequency intercept (LF$_{int}$) with the real photocurrent axis:

$$LF_{int} = \frac{k_{tr}}{k_{tr} + k_{rec}} \qquad (19)$$

Using eqn (18) and (19), both k_{tr} and k_{rec} can therefore be determined. Details of the model (assumptions, limitations, etc.) and the derivation of the equations can be found in the literature.[36,37]

It is important to note that care should be taken in interpreting the absolute value of k_{tr} and k_{rec}. For a simple one-electron charge transfer reaction, these rate constants are true rate constants
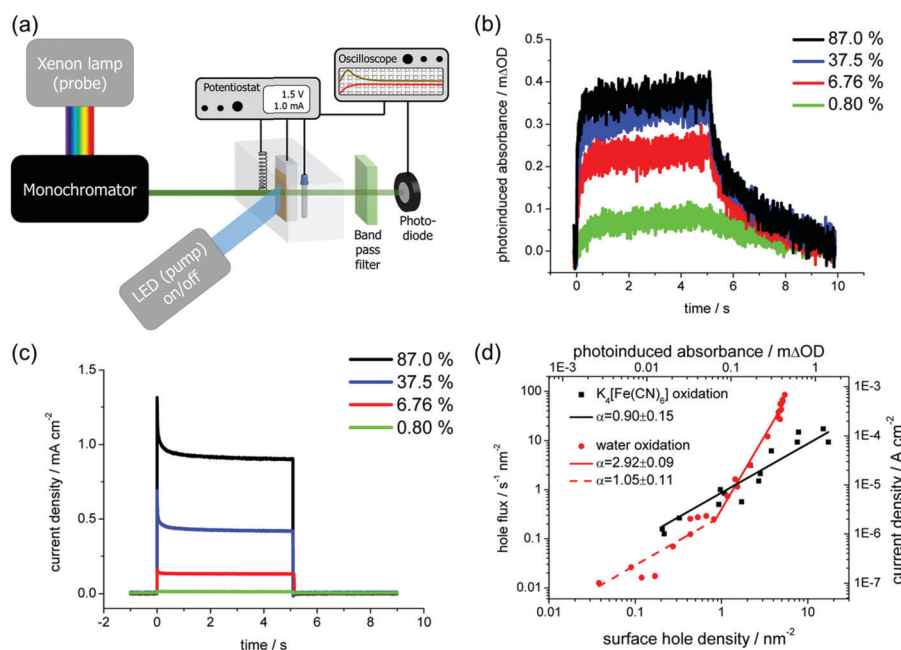
Fig. 12 (a) Schematic illustration of a typical photoinduced absorption (PIA) spectroscopy setup. (b) PIA signal and (c) photocurrent density of a $BiVO_4$ photoanode simultaneously measured under 5 s pulsed 365 nm LED illumination (with varying illumination intensity—100% corresponds to the intensity of AM1.5 illumination) under water oxidation conditions at 1.7 V vs. RHE. (d) Relationship between the photocurrent density and the surface hole density (determined from the PIA signal). Fitting the data with a kinetic model reveals the reaction order (α) for water oxidation on $BiVO_4$. Figure b–d: reproduced from ref. 35 with permission from the American Chemical Society, copyright 2016.

This journal is © The Royal Society of Chemistry 2019

Chem. Soc. Rev., 2019, **48**, 1255–1271 | **1267**
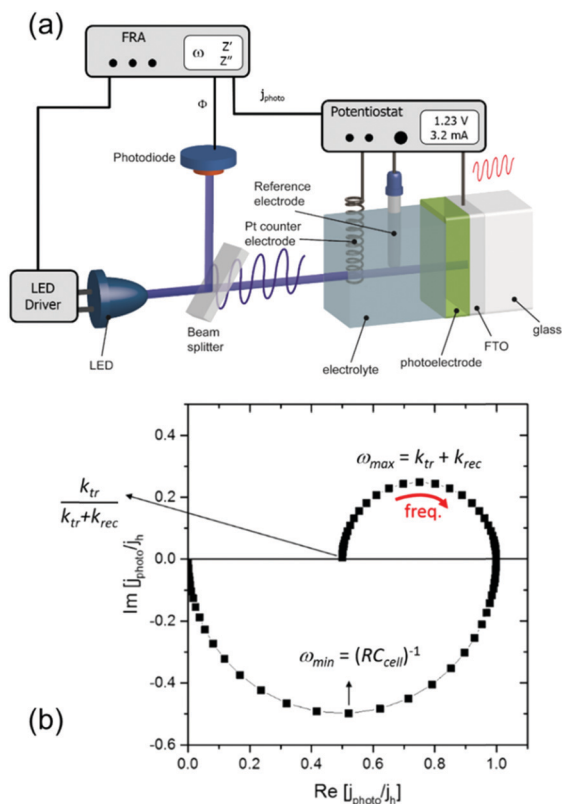
Fig. 13 (a) Schematic diagram of a typical IMPS setup. (b) An example of a complex photocurrent or an IMPS spectrum for an n-type semiconductor. The recombination semicircle is shown in the upper quadrant, and the attenuation semicircle appears in the lower quadrant. Using a model of Peter *et al.*,[36] the charge transfer rate constant (k_{tr}) and the surface recombination rate constant (k_{rec}) can be obtained based on the multiple points of such a spectrum. Figure a and b: reproduced from ref. 37 with permission from The Royal Society of Chemistry, copyright 2017.

(the unit is s^{-1}). It is however more complicated for the case of multi-step charge transfer reactions, such as water oxidation and reduction. In this case, k_{tr} and k_{rec} should be interpreted as phenomenological rate parameters that are functions of the rate constants of the elementary steps.[38] If the reaction mechanism is known, the relationship can in principle be derived,[38] but this has not been attempted, especially for the water oxidation reaction. Nevertheless, the equations above can still be used to analyze the IMPS response and distinguish charge transfer and recombination processes. k_{tr} and k_{rec} are therefore usually called pseudo first-order rate constants in the literature.[37]

5. Combinatorial/*in situ* approaches

Most of the characterization tools discussed in Sections 2–4 are macroscopic, that is, the measured properties are generally the averages of the bulk sample that may not be representative of the isolated/local microstructures. Typically, the properties of a semiconductor photo(electro)catalyst do not only rely on the bulk composition but also greatly on the surface crystallinity

and structure such as the surface atomic arrangement and coordination. With the pre-eminence of nanomaterials in photo-(electro)catalysis, advancement of research tools with high selectivity, sensitivity, and spatial resolution is essential to provide direct experimental evidence for surface-dependent properties *via* micro-region measurements. In particular, more than one tool can be combined to provide more comprehensive insight into various aspects of the photo(electro)catalyst. For example, a light source can be incorporated into a conductive atomic force microscope (*i.e.*, photoassisted conductive atomic force microscopy PC-AFM) to enable local determination of the optoelectronic and the interfacial charge transfer properties of a photocatalyst.[39] Coupling of spatially resolved surface photovoltage spectroscopy (SRSPS) with Kelvin probe force microscopy (KPFM) has been demonstrated to be useful in showing the highly anisotropic photoinduced charge separation on the different crystal facets of a single photocatalyst.[40] The combination of optical and electrochemical techniques such as spatially and temporally resolved single-particle spectroelectrochemistry is also helpful in revealing the carrier dynamics of a photocatalyst in relation to its crystal faces.[41]

Another major downside of the techniques outlined in preceding sections is that the measurements are typically done before and after the photocatalytic or photoelectrochemical reaction. This greatly obscures the understanding of the structure–property relationship that could potentially change during the reaction. *In situ* techniques have thus come forth in order to obtain a direct relationship between the optoelectronic/electrochemical and the physicochemical properties (*e.g.*, particle size, crystallinity, morphology, crystal structure, and surface chemical states) of a semiconductor (down to nanosize scale) during a reaction. One great example in line with the scope of this review is the engineering of *in situ* transmission electron microscopy (TEM),[42,43] whereby the TEM column or specimen holder is modified to enable light illumination and/or emitted light collection to enable real-time measurements of nanostructure properties in response to light in tandem with high resolution imaging of the material. Fig. 14a illustrates the schematic of a typical opto-TEM setup that enables *in situ* illumination and light collection by incorporating a combination of mirrors, lenses, and optical fibers into the TEM column. Detailed explanation of the setup is described elsewhere.[42] Such a system has also been demonstrated to produce a smaller light probe (10 μm in diameter) with near-field light by positioning a silver-coated tungsten tip normal to the optical path of laser light (Fig. 14b).[43] Without modification to the TEM column, light transmission can also be achieved using an opto-compatible TEM holder, in which lenses or optical fibers are integrated. Accessibility to various opto-compatible TEM holders and opto-TEM setups has made *in situ* PL, Raman, and photocurrent spectroscopy measurements inside TEM viable.

In situ and *operando* X-ray powder diffraction (XRD) and ambient-pressure photoemission spectroscopy measurements under operating (photo)electrochemical conditions have also been carried out recently. Fig. 14c shows an *operando* synchrotron XRD setup using a tailor-made doughnut shaped photoelectrochemical

1268 | *Chem. Soc. Rev.*, 2019, **48**, 1255–1271

This journal is © The Royal Society of Chemistry 2019
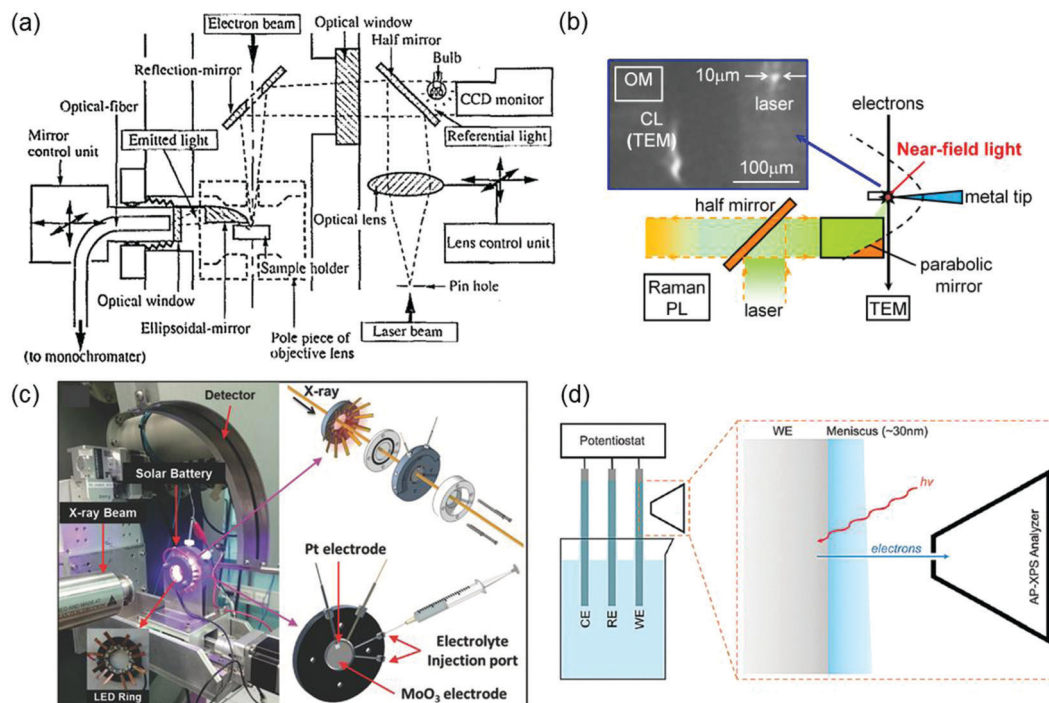
Fig. 14   (a) Schematic of a typical opto–TEM setup with *in situ* illumination and emitted light collection. Reproduced from ref. 42 with permission from the AIP Publishing, copyright 1995. (b) An opto–TEM setup with *in situ* near–field photoexcitation. Reproduced from ref. 43 with permission from Elsevier B.V., copyright 2013. (c) *Operando* XRD setup with a customized LED integrated photoelectrochemical cell. Reproduced from ref. 44 with permission from WILEY–VCH Verlag GmbH & Co. KGaA, Weinheim, copyright 2017. (d) A typical three–electrode electrochemical setup for AP–XPS measurement of a working electrode (WE) surface covered by a meniscus layer of the electrolyte. RE: reference electrode; CE: counter electrode. Reproduced from ref. 45 with permission from the PCCP Owner Societies, copyright 2015.

cell. While the LED integrated open center cell enables illumination of the solar battery consisting of MoO_3 and Pt as the respective photoanode and counter electrodes, *in situ* XRD measurement allows real-time visualization of the structural evolution of MoO_3 due to light-induced photointercalation.[44] The development of ambient-pressure XPS (AP-XPS), on the other hand, allows *in situ* characterization of electrode/electrolyte interfaces that are crucial in (photo)electrochemical systems.[45,46] A typical setup of AP-XPS is illustrated in Fig. 14d. In particular, the use of tender X-rays with energies between soft and hard X-rays ($\sim$2–7 keV) facilitates *operando* XPS characterization of the chemical changes at the electrode/electrolyte interfaces. However, due to the limited photoelectron mean free path, the electrolyte thickness in such ambient-pressure tender XPS method needs to be kept in the range of 20–30 nm. One common approach to obtain a thin layer of electrolyte film is *via* the dip-and-pull technique, whereby the working electrode is dipped and pulled from the electrolyte reservoir therefore creating an electrolyte meniscus (see Fig. 14d).

6. Summary

An overview of the current experimental techniques accessible for scrutinizing the three discrete key properties of a photo-active semiconductor, including the band gap (E_g), absolute

potentials of the conduction band minimum (E_{CB}) and the valence band maximum (E_{VB}), and charge carrier dynamics within the bulk and at the surface of the semiconductor (*i.e.*, diffusion length L_D, mobility μ, lifetime τ, surface charge recombination rate, and interfacial charge transfer rate), is provided. Technology advancement, mainly in the past few decades, has enabled the development of various sophisticated characterization tools with high spatial, temporal, and spectral resolutions as well as high sensitivity and selectivity. Although we intended to present state-of-the-art experimental characterization techniques in addition to the common methods related to the determination of all key aspects of photo(electro)-catalysts, it should be realized that the list of measurement techniques described herein is not exhaustive. For instance, time-resolved THz spectroscopy has been used to investigate the bulk charge carrier dynamics (*i.e.*, to determine μ and τ),[28] and photoelectrochemical impedance spectroscopy (PEIS) has been widely used to determine the rate constants for the processes at the semiconductor/electrolyte interface.[47] Readers are recommended to refer to the excellent review papers and books that provided details of these additional techniques.[48–50]

Note that despite the restriction of several methods to electrode-based systems, they are generally applicable for measurements on particulate materials by proper transformation of the powders into thin films on suitable substrates since the attained properties are often transferable to particle-based

This journal is © The Royal Society of Chemistry 2019

Chem. Soc. Rev., 2019, **48**, 1255–1271 | **1269**

systems. Given the inherent limitations of each macroscopic technique, a combination of numerous analysis approaches is typically essential to provide a more complete and concrete evaluation of the specific aspect of a semiconductor. In particular, direct measurements of local optoelectronic properties and charge carrier dynamics in relation to the surface structure of nanostructures have been demonstrated to be feasible. The breakthrough of experimental characterization tools is undoubtedly the invention of *in situ* and/or *operando* measurements, allowing real-time evaluation of semiconductor properties.

Conflicts of interest

The authors declare no conflict of interest.

Acknowledgements

References

1 H. L. Tan, R. Amal and Y. H. Ng, *J. Mater. Chem. A*, 2017, **5**, 16498–16521.

2 S. Tandon and J. Gupta, *Phys. Status Solidi B*, 1970, **38**, 363–367.

3 J. Tauc, in *Optical Properties of Solids* ed. F. Abeles, North-Holland Publ. Co, Amsterdam, 1972.

4 E. Davis and N. Mott, *Philos. Mag.*, 1970, **22**, 0903–0922.

5 J. H. Nobbs, *Color. Technol.*, 1985, **15**, 66–75.

6 L. Kronik and Y. Shapira, *Surf. Interface Anal.*, 2001, **31**, 954–965.

7 L. Kronik and Y. Shapira, *Surf. Sci. Rep.*, 1999, **37**, 1–206.

8 M. Anpo and M. Che, *Advances in Catalysis*, Elsevier, 1999, vol. 44, pp. 119–257.

9 C. Li and Y. Yue, *Nanotechnology*, 2014, **25**, 435703.

10 S. R. Morrison, *Electrochemistry at semiconductor and oxidized metal electrodes*, Springer, US, 1980.

11 R. Beranek, *Adv. Phys. Chem.*, 2011, **2011**, 786759.

12 D. Cahen and A. Kahn, *Adv. Mater.*, 2003, **15**, 271–277.

13 M. Jakob, H. Levanon and P. V. Kamat, *Nano Lett.*, 2003, **3**, 353–358.

14 N. Dimitrijevic, D. Savic, O. Micic and A. Nozik, *J. Phys. Chem.*, 1984, **88**, 4278–4283.

15 J. Gandia, M. Pujadas and P. Salvador, *J. Electroanal. Chem. Interfacial Electrochem.*, 1988, **244**, 69–79.

16 E. Kraut, R. Grant, J. Waldrop and S. Kowalczyk, *Phys. Rev. Lett.*, 1980, **44**, 1620.

17 S. A. Chambers, T. Droubay, T. C. Kaspar and M. Gutowski, *J. Vac. Sci. Technol., B: Microelectron. Nanometer Struct.--Process., Meas., Phenom.*, 2004, **22**, 2205–2215.

18 W.-J. Chun, A. Ishikawa, H. Fujisawa, T. Takata, J. N. Kondo, M. Hara, M. Kawai, Y. Matsumoto and K. Domen, *J. Phys. Chem. B*, 2003, **107**, 1798–1803.

19 S. Trasatti, *Pure Appl. Chem.*, 1986, **58**, 955–966.

20 S. S. Li, *Appl. Phys. Lett.*, 1976, **29**, 126–127.

21 M. Saritas and H. D. McKell, *J. Appl. Phys.*, 1988, **63**, 4561–4567.

22 T. Dittrich, F. Lang, O. Shargaieva, J. Rappich, N. Nickel, E. Unger and B. Rech, *Appl. Phys. Lett.*, 2016, **109**, 073901.

23 C. Wu and D. Wittry, *J. Appl. Phys.*, 1978, **49**, 2827–2836.

24 T. Gokmen, O. Gunawan and D. B. Mitzi, *J. Appl. Phys.*, 2013, **114**, 114511.

25 R. A. Pala, A. J. Leenheer, M. Lichterman, H. A. Atwater and N. S. Lewis, *Energy Environ. Sci.*, 2014, **7**, 3424–3430.

26 A. J. Rettie, W. D. Chemelewski, D. Emin and C. B. Mullins, *J. Phys. Chem. Lett.*, 2016, 7, 471–479.

27 O. Gunawan, S. R. Pae, D. M. Bishop, Y. S. Lee, Y. Virgus, N. J. Jeon, J. H. Noh, X. Shao, T. Todorov and D. B. Mitzi, 2018, arXiv preprint arXiv:1802.07910.

28 M. Ziwritsch, S. Müller, H. Hempel, T. Unold, F. F. Abdi, R. van de Krol, D. Friedrich and R. Eichberger, *ACS Energy Lett.*, 2016, **1**, 888–894.

29 D. Emin, in *The Hall Effect and Its Applications*, ed. C. L. Chien and C. R. Westgate, Springer, Boston, MA, 1980, pp. 281–298.

30 T. J. Savenije, A. J. Ferguson, N. Kopidakis and G. Rumbles, *J. Phys. Chem. C*, 2013, **117**, 24085–24103.

31 F. F. Abdi, T. J. Savenije, M. M. May, B. Dam and R. van de Krol, *J. Phys. Chem. Lett.*, 2013, **4**, 2752–2757.

32 J. W. Jang, D. Friedrich, S. Müller, M. Lamers, H. Hempel, S. Lardhi, Z. Cao, M. Harb, L. Cavallo and R. Heller, *Adv. Energy Mater.*, 2017, **7**, 1701536.

33 H. K. Dunn, L. M. Peter, S. J. Bingham, E. Maluta and A. B. Walker, *J. Phys. Chem. C*, 2012, **116**, 22063–22072.

34 S. R. Pendlebury, M. Barroso, A. J. Cowan, K. Sivula, J. Tang, M. Grätzel, D. Klug and J. R. Durrant, *Chem. Commun.*, 2011, **47**, 716–718.

35 Y. Ma, C. A. Mesa, E. Pastor, A. Kafizas, L. Francàs, F. Le Formal, S. R. Pendlebury and J. R. Durrant, *ACS Energy Lett.*, 2016, **1**, 618–623.

36 E. Ponomarev and L. Peter, *J. Electroanal. Chem.*, 1995, **396**, 219–226.

37 C. Zachäus, F. F. Abdi, L. M. Peter and R. van De Krol, *Chem. Sci.*, 2017, **8**, 3712–3719.

38 L. Peter, E. Ponomarev and D. Fermin, *J. Electroanal. Chem.*, 1997, **427**, 79–96.

39 S. Wang, X. Zhang, G. Cheng, X. Jiang, Y. Li, Y. Huang and Z. Du, *Chem. Phys. Lett.*, 2005, **405**, 63–67.

40 J. Zhu, F. Fan, R. Chen, H. An, Z. Feng and C. Li, *Angew. Chem.*, 2015, **127**, 9239–9242.

41 T. Tachikawa, T. Ochi and Y. Kobori, *ACS Catal.*, 2016, **6**, 2250–2256.

42 Y. Ohno and S. Takeda, *Rev. Sci. Instrum.*, 1995, **66**, 4866–4869.

43 Y. Ohno and I. Yonenaga, *Appl. Surf. Sci.*, 2014, **302**, 29–31.

44 S. N. Lou, N. Sharma, D. Goonetilleke, W. H. Saputera, T. M. Leoni, P. Brockbank, S. Lim, D. W. Wang, J. Scott and R. Amal, *Adv. Energy Mater.*, 2017, **7**, 1700545.

1270 | *Chem. Soc. Rev.*, 2019, **48**, 1255–1271

This journal is © The Royal Society of Chemistry 2019

45 C. H. Wu, R. S. Weatherup and M. B. Salmeron, *Phys. Chem. Chem. Phys.*, 2015, **17**, 30229–30239.

46 D. E. Starr, M. Favaro, F. F. Abdi, H. Bluhm, E. J. Crumlin and R. van de Krol, *J. Electron Spectrosc. Relat. Phenom.*, 2017, **221**, 106–115.

47 B. Klahr, S. Gimenez, F. Fabregat-Santiago, J. Bisquert and T. W. Hamann, *J. Am. Chem. Soc.*, 2012, **134**, 16693–16700.

48 R. Ulbricht, E. Hendry, J. Shan, T. F. Heinz and M. Bonn, *Rev. Mod. Phys.*, 2011, **83**, 543.

49 L. Bertoluzzi and J. Bisquert, *J. Phys. Chem. Lett.*, 2012, **3**, 2517–2522.

50 E. Barsoukov and J. R. Macdonald, *Impedance Spectroscopy: Theory, Experiment, and Applications*, John Wiley & Sons, Hoboken, NJ, 2018.

This journal is © The Royal Society of Chemistry 2019

Chem. Soc. Rev., 2019, **48**, 1255–1271 | **1271**